Electronic Supplementary Material (ESI) for Physical Chemistry Chemical Physics.

Electronic Supplementary Information

Anti-Ohmic Nanoconductors: Myth, Reality and Promise

Ashima Bajaj and Md. Ehesan Ali*

Institute of Nano Science and Technology, Sector-81, Mohali-140306, Punjab, India

E-mail: ehesan.ali@inst.ac.in

Contents

1 Computational details **S3**

2 Computed energies in different electronic states **S5**

3 Computed $<S^2>$ values and radicaloid character **S7**

4 Central subsystem frontier orbitals **S10**

5 Frontier orbitals for isolated molecules **S12**

6 Spin density distribution **S15**

7 Energetics of molecular states **S18**

8 CAM-B3LYP computed conductance **S19**

9 Bond Length Alternation **S25**

1 Computational details

Isolated molecule geometry optimization: Geometry optimization of isolated molecules are first performed by applying B3LYP[1] hybrid functional and def2-TZVP[2] basis set in two distinct electronic states, i.e., closed shell singlet (CSS) and broken symmetry open shell singlet (OSS) state in ORCA[3] quantum chemical code. OSS states are treated using spin-unrestricted broken-symmetry Kohn-Sham (UKS-BS) method within the DFT framework, while spin-restricted (RKS) wavefunction is used for CSS states. Resolution of the identity (RI) approximation in conjunction with auxiliary basis set def2/J and chain of spheres (COSX) numerical integration is used to accelerate the calculations without losing its accuracy.[4] Tight convergence limits and increased integration grids (grid5) are used throughout. Isolated molecules are further re-optimized by including the two S-H bonds at both the ends using B3LYP/def2-TZVP method. We found that the electronic structure of isolated molecule is little affected by the inclusion of S-H end groups. As illustrated in Table S1 to S4, molecule retains its same ground state with thiol end groups as of molecules without thiol groups.

Construction of Gold-Molecule-Gold junction: The molecular junctions are then constructed by placing the optimized isolated dithiol molecules between two gold electrodes after removing the terminal hydrogen atoms of thiol groups and forming the S-Au bonds. The gold electrodes are approximated by nine-atomic gold clusters, arranged in hexagonal closed-packed fcc Au-111 surface. The Au-Au distance is set to 2.88 Å and Au-S distance is fixed to 2.40 Å, which is similar to our previous reported works.[5,6]

Transport calculations: For computing the transmission probability as a function of energy, first single point calculations are carried out for molecular junction using B3LYP functional and LANL2DZ[7] basis set to extract the Hamiltonian and overlap matrices required for transport calculations. The transmission functions are then obtained using NEGF-DFT based post-processing tool *Artaios*.[8]

In the Green's function approach[9] employed here, the transmission function T(E) is obtained as the trace of coupling matrices ($\Gamma_{L/R}$) describing the coupling of central region to the left and right electrodes and the retarted/advanced Green's function ($G/G^{\dagger}$) of cluster-molecule-cluster system, written as

$$T_{\sigma}(E) = Tr(\Gamma_R G \Gamma_L G^{\dagger})_{\sigma} \tag{1}$$

where σ represents the spin up/down electrons. The coupling matrices, $\Gamma_{L/R}$, are calculated from the imaginary parts of the corresponding self-energies, $\Sigma_{L,R}$, as

$$\Gamma_{L,R} = \iota(\Sigma_{L,R} - \Sigma_{L,R}^{\dagger}) \tag{2}$$

which in turn are obtained from overlap and Fock matrices as

$$\Sigma_{L,R} = (ES_{LC/RC} - H_{LC/RC})^{\dagger} g_{L/R} (ES_{LC/RC} - H_{LC/RC}) \tag{3}$$

The retarded green's function is calculated as

$$G(E) = (ES_M - H_M - \Sigma_L - \Sigma_R)^{-1} \tag{4}$$

The Fock and overlap matrices are divided into central, left-electrode, and right-electrode regions. $S_{LC/RC}$ and $H_{LC/RC}$ denote the coupling block of L/R electrode and molecule in the overlap and Fock matrices respectively, while S_M and H_M indicates central molecule subblocks. The green's function matrices of the electrode ($g_{L/R}$) is calculated in wide-band-limit (WBL) approximation as

$$g_{L/R} = -\iota.\pi.DOS^{const.}.\delta_{ij} \tag{5}$$

which assumes a constant density of states, independent of energy. A constant value of 0.036 ev^{-1}, taken from literature is used for the DOS of electrode.[10]

2 Computed energies in different electronic states

Table S1: Computed energies for **isolated acenes** (n = 1 to 12) in the closed shell singlet (CSS) using B3LYP/def-TZVP method and open shell singlet (OSS) states using UB3LYP/def2-TZVP method and relative energy difference $\Delta E_{OSS-CSS}$. Absolute energies are given in Hartrees for CSS and OSS states, whereas $\Delta E_{OSS-CSS}$ is given in eV.

Acenes (n)	**E(CSS)** (Hartrees)	**E(OSS)** (Hartrees)	Δ**E**$_{OSS-CSS}$ (eV)
1	-232.183332	-232.183332	0.000
2	-385.783010	-385.783010	0.000
3	-539.376500	-539.376500	0.000
4	-692.967574	-692.967574	0.000
5	-846.557436	-846.557436	0.000
6	-1000.146651	-1000.146719	-0.001
7	-1153.735480	-1153.737881	-0.065
8	-1307.324086	-1307.330339	-0.170
9	-1460.912713	-1460.923095	-0.280
10	-1614.501478	-1614.516031	-0.394
11	-1768.083119	-1768.108186	-0.680
12	-1921.676179	-1921.700245	-0.653

Table S2: Computed energies for **isolated acenes with thiol terminating groups** (n = 1 to 12) in the closed shell singlet (CSS) using B3LYP/def2-TZVP method and open shell singlet (OSS) states using UB3LYP/def2-TZVP method and relative energy difference $\Delta E_{OSS-CSS}$. Absolute energies are given in Hartrees for CSS and OSS states, whereas $\Delta E_{OSS-CSS}$ is given in eV.

Acenes (n) (Thiol group)	**E(CSS)** (Hartrees)	**E(OSS)** (Hartrees)	Δ**E**$_{OSS-CSS}$ (eV)
1	-1028.497473	-1028.497473	0.000
2	-1182.097546	-1182.097546	0.000
3	-1335.691834	-1335.691838	0.000
4	-1489.283043	-1489.283043	0.000
5	-1642.873063	-1642.873062	0.000
6	-1796.462404	-1796.462405	0.00
7	-1950.050560	-1950.052660	-0.057
8	-2103.640000	-2103.645633	-0.153
9	-2257.228377	-2257.238334	-0.271
10	-2410.818261	-2410.831941	-0.370
11	-2564.397510	-2564.422191	-0.669
12	-2717.991801	-2718.015746	-0.650

Table S3: Computed energies for **isolated cumulenes substituted with phenyl groups at both the ends** ($n = 4$ to 24) in the closed shell singlet (CSS) using B3LYP/def2-TZVP method and open shell singlet (OSS) states using UB3LYP/def2-TZVP method and relative energy difference $\Delta E_{OSS-CSS}$. Absolute energies are given in Hartrees for CSS and OSS states, whereas $\Delta E_{OSS-CSS}$ is given in eV.

Cumulenes	**E(CSS)** (Hartrees)	**E(OSS)** (Hartrees)	Δ**E**$_{OSS-CSS}$ (eV)
C4	-1078.661716	-1078.661167	0.000
C6	-1154.799128	-1154.799125	0.000
C8	-1230.939915	-1230.939900	0.004
C10	-1307.081285	-1307.081273	0.003
C12	-1383.224218	-1383.224314	-0.002
C14	-1459.366418	-1459.367005	-0.015
C16	-1535.509138	-1535.510271	-0.030
C18	-1611.652149	-1611.654076	-0.052
C20	-1687.795339	-1687.798150	-0.076
C22	-1763.936994	-1763.940922	-0.106
C24	-1840.079676	-1840.084684	-0.138

Table S4: Computed energies for **isolated phenyl-substituted cumulenes with thiol anchoring groups** ($n = 4$ to 24) in the closed shell singlet (CSS) using B3LYP/def2-TZVP method and open shell singlet (OSS) states using UB3LYP/def2-TZVP method and relative energy difference $\Delta E_{OSS-CSS}$. Absolute energies are given in Hartrees for CSS and OSS states, whereas $\Delta E_{OSS-CSS}$ is given in eV.

Cumulenes (Thiol group)	**E(CSS)** (Hartrees)	**E(OSS)** (Hartrees)	Δ**E**$_{OSS-CSS}$ (eV)
C4	-1874.977405	-1874.977404	0.000
C6	-1951.115731	-1951.115733	0.000
C8	-2027.256942	-2027.256940	0.000
C10	-2103.398376	-2103.398370	0.000
C12	-2179.541382	-2179.541503	-0.003
C14	-2255.683584	-2255.684456	-0.023
C16	-2331.826171	-2331.827964	-0.048
C18	-2407.969180	-2407.972006	-0.076
C20	-2484.112453	-2484.116482	-0.109
C22	-2560.254403	-2560.259939	-0.150
C24	-2636.396995	-2636.403884	-0.187

3 Computed $<S^2>$ values and radicaloid character

Spin expectation value: The $<S^2>$ values of broken symmetry spin-unrestricted wave-function for acenes and cumulenes are tabulated in Table S5 - S6 in both gas phase and in molecular junction. Broken symmetry solution is a $M_s = 0$ solution ,i.e., a mixture of singlet and triplet states. If the singlet-triplet energy gap in a singlet diradical is small, the BS wave function contains singlet and triplet wave functions with equal weights. Therefore, a spin expectation value near 1.0 is expected for a pronounced singlet diradical. If the mean value of $<S^2>$ of the Ms = 0 solution is larger than 1, it indicates the contribution from the excited states of higher spin multiplicity. For the lower members of the series, $<S^2>_{BS} = 0$ indicates that BS solution do no exist and hence diradical character is zero. As the length is increased, $<S^2>_{BS}$ monotonically increases in all the cases in such a way that $<S^2>_{BS}$ tends to 1 indicating a perfect diradical states for those cases. Further, only a slight change in observed in $<S^2>$ values upon placing the molecules in junctions, indicating that the molecule retains its same ground state in junction as in isolated gas phase.

Table S5: Computed $<S^2>$ values in broken symmetry states ($<S^2>_{BS}$) at UB3LYP/def2-TZVP level for isolated acenes and acenes in junction (n = 1 to 12) with both para and meta connections.

Acenes (n)	$<S^2>_{BS}$		
	Isolated Molecule	Junction(para)	Junction(meta)
1	0.00	0.00	0.00
2	0.00	0.00	0.00
3	0.00	0.00	0.00
4	0.00	0.00	0.00
5	0.00	0.00	0.00
6	0.15	0.00	0.00
7	0.77	0.67	0.67
8	1.07	0.96	0.99
9	1.24	1.19	1.18
10	1.39	1.35	1.36
11	1.54	1.50	1.50
12	1.71	1.68	1.69

Table S6: Computed $<S^2>$ values in broken symmetry states ($<S^2>_{BS}$) at UB3LYP/def2-TZVP level for phenyl-substituted cumulenes ($C4$ to $C24$) in gas phase and in molecular junction.

Cumulenes (n)	$<S^2>_{BS}$	
	Isolated Molecule	Junction
C4	0.00	0.00
C6	0.00	0.00
C8	0.00	0.00
C10	0.01	0.00
C12	0.15	0.25
C14	0.37	0.57
C16	0.54	0.77
C18	0.72	0.92
C20	0.91	1.04
C22	1.09	1.13
C24	1.26	1.20

Radicaloid character: (y) To estimate the extent of increasing radical character with length in both acenes and cumulenes, we quantified the radicaloid character (y-value) from the occupancy of UHF based orbitals as proposed by Yamaguchi et al., using Eq. 6

$$y = 1 - \frac{2T}{1+T^2} \tag{6}$$

where,

$$T = \frac{n_{HOMO} - n_{LUMO}}{2} \tag{7}$$

where n_{HOMO} and n_{LUMO} are the occupancies of the frontier natural orbitals. To evaluate y, BS calculations with unrestricted Hartree-Fock (UHF) using a def2-TZVP basis set are performed using ground state geometry, i.e., RKS optimized geometry is used for lower members of the series with CSS ground state, while UKS-BS optimized geometry is used for higher members with OSS ground state. The similar methodology is also employed in our previous works.[11,12] The occupancy of highest occupied n_{HOMO} and lowest unoccupied n_{LUMO} and the calculated radicaloid character y are tabulated in Table S7 and Table S8 for acenes and cumulenes respectively. It reveals that the occupancy of frontier HONO and

LUNO orbitals tends to approach one instead of two for n >7 acenes.

Thus indicating the presence of two nearly singly occupied frontier orbitals and hence the open shell singlet character. Apart from the HONO and LUNO, the similar trend is present to a lower degree for next nearest orbitals, i.e., HONO-1 and LUNO+1, with an increasing occupation number of LUNO+1 and a decreasing of that of HONO-1. For n = 11, the occupation numbers of HONO-1 (1.29) and LUNO+1 (0.70) indeed support the idea of tetra-radical character, with four nearly singly occupied open shells.

Table S7: Calculated radicaloid character (y) for polyacenes (n = 1 to 12) and occupancy of frontier highest occupied (n_{HONO}), lowest unoccupied (n_{LUNO}), next nearest HONO-1 (n_{HONO-1}) and LUNO+1 (n_{LUNO+1}) BS- UHF orbitals calculated using def2-TZVP Method.

Acenes (n)	n_{HONO-1}	n_{HONO}	n_{LUNO}	n_{LUNO+1}	y
1	1.90	1.90	0.09	0.09	0.005
2	1.84	1.74	0.25	0.15	0.04
3	1.82	1.58	0.41	0.17	0.13
4	1.78	1.44	0.55	0.21	0.26
5	1.70	1.33	0.66	0.29	0.39
6	1.61	1.24	0.75	0.38	0.53
7	1.53	1.15	0.84	0.46	0.75
8	1.46	1.10	0.89	0.53	0.80
9	1.39	1.06	0.93	0.60	0.87
10	1.34	1.03	0.96	0.65	0.93
11	1.29	1.01	0.98	0.70	0.97
12	1.24	1.00	0.99	0.75	0.99

Table S8: Calculated radicaloid character (y) for phenyl-substituted cumulenes ($C4$ to $C24$) along with the occupancy of frontier highest occupied (n_{HONO}), lowest unoccupied (n_{LUNO}), next nearest HONO-1 (n_{HONO-1}) and LUNO+1 (n_{LUNO+1}) BS-UHF orbitals calculated using def2-TZVP Method.

Cumulenes					
n	n_{HONO-1}	n_{HONO}	n_{LUNO}	n_{LUNO+1}	y
C4	1.86	1.47	0.52	0.13	0.22
C6	1.77	1.37	0.62	0.22	0.34
C8	1.63	1.29	0.70	0.36	0.45
C10	1.52	1.24	0.75	0.47	0.53
C12	1.46	1.20	0.79	0.53	0.60
C14	1.43	1.15	0.84	0.56	0.69
C16	1.40	1.12	0.87	0.59	0.75
C18	1.37	1.10	0.89	0.62	0.79
C20	1.36	1.08	0.91	0.63	0.83
C22	1.35	1.06	0.93	0.64	0.87
C24	1.34	1.05	0.94	0.65	0.89

4 Central subsystem frontier orbitals

The frontier orbital energies of cluster-molecule-cluster model for all the systems are obtained from central subsytem molecular orbitals. Following the methodology by Herrmann et al,[10] central subsystem MOs are evaluated by solving the secular equation for the central subsystem block of the Hamiltonian matrix (here, only molecule constitutes the central region). Since, peaks in transmission spectra are located at the energies of the central subsystem MOs, therefore, only subsystem MOs are analyzed rather than full junction MOs which are similar in shape but slightly shifted in energy due to renormalization of molecular electronic levels in molecular junction.[13] The designation of HOMO and LUMO is made by comparing the central subsystem MOs with the isolated molecule HOMO and LUMO orbitals. Since, we have set the Fermi level of the electrodes to -4.00 eV throughout this work, thus the frontier orbital energies are also shifted against the estimated Fermi energy of -4.00 eV.

Table S9: Energies of central subsystem frontier HOMO and LUMO orbitals and the corresponding energy gap ΔE_{HL} for meta connected acenes placed between two Au_9 clusters in CSS and OSS state. The energies of the orbitals are shifted against estimated Fermi energy of -4 eV.

***m*-acenes**	**CSS state**			**OSS state**		
n	E(HOMO)	E(LUMO)	ΔE_{HL}	E(HOMO)	E(LUMO)	ΔE_{HL}
1	-3.37	3.23	**6.60**	-3.37	3.23	**6.60**
2	-2.43	2.35	**4.78**	-2.43	2.35	**4.78**
3	-1.80	1.81	**3.61**	-1.80	1.81	**3.61**
4	-1.38	1.43	**2.81**	-1.38	1.43	**2.81**
5	-1.09	1.17	**2.26**	-1.09	1.17	**2.26**
6	-0.85	0.98	**1.83**	-0.86	0.98	**1.84**
7	-0.63	0.79	**1.42**	-0.83	0.97	**1.80**
8	-0.48	0.67	**1.15**	-0.79	0.98	**1.77**
9	-0.37	0.58	**0.95**	-0.77	1.00	**1.77**
10	-0.28	0.52	**0.80**	-0.77	1.00	**1.77**
11	-0.21	0.48	**0.69**	-0.76	1.03	**1.79**
12	-0.16	0.35	**0.51**	-0.78	1.06	**1.84**

Table S10: Energies of central subsystem frontier HOMO and LUMO orbitals and the corresponding energy gap ΔE_{HL} for para connected acenes placed between two Au_9 clusters in CSS and OSS state. The energies of the orbitals are shifted against estimated Fermi energy of -4 eV.

***p*-acenes**	**CSS state**			**OSS state**		
n	E(HOMO)	E(LUMO)	ΔE_{HL}	E(HOMO)	E(LUMO)	ΔE_{HL}
1	-3.07	3.32	**6.39**	-3.07	3.32	**6.39**
2	-2.40	2.36	**4.76**	-2.40	2.36	**4.76**
3	-1.79	1.82	**3.61**	-1.79	1.82	**3.61**
4	-1.36	1.45	**2.81**	-1.36	1.45	**2.81**
5	-1.07	1.19	**2.26**	-1.09	1.19	**2.26**
6	-0.84	1.00	**1.84**	-0.84	1.00	**1.84**
7	-0.61	0.81	**1.42**	-0.80	1.01	**1.81**
8	-0.47	0.73	**1.20**	-0.79	1.01	**1.80**
9	-0.36	0.59	**0.95**	-0.79	1.02	**1.81**
10	-0.26	0.53	**0.80**	-0.77	1.04	**1.81**
11	-0.13	0.34	**0.47**	-0.75	1.04	**1.79**
12	-0.14	0.37	**0.51**	-0.76	1.05	**1.81**

Table S11: Energies of central subsystem frontier HOMO and LUMO orbitals and the corresponding energy gap ΔE_{HL} for phenyl-substituted cumulenes placed between two Au_9 clusters in CSS and OSS state. The energies of the orbitals are shifted against estimated Fermi energy of -4 eV.

Cumulenes	**CSS state**			**OSS state**		
n	E(HOMO)	E(LUMO)	ΔE_{HL}	E(HOMO)	E(LUMO)	ΔE_{HL}
C4	-1.03	1.93	**2.96**	-1.03	1.93	**2.96**
C6	-0.89	1.61	**2.50**	-0.89	1.61	**2.50**
C8	-0.80	1.27	**2.07**	-0.80	1.27	**2.07**
C10	-0.73	1.11	**1.84**	-0.73	1.11	**1.84**
C12	-0.70	0.95	**1.65**	-0.73	1.11	**1.73**
C14	-0.56	0.74	**1.30**	-0.72	0.90	**1.62**
C16	-0.55	0.61	**1.16**	-0.78	0.84	**1.62**
C18	-0.51	0.51	**1.02**	-0.79	0.80	**1.59**
C20	-0.47	0.41	**0.87**	-0.81	0.73	**1.54**
C22	-0.40	0.33	**0.73**	-0.76	0.69	**1.45**
C24	-0.35	0.29	**0.63**	-0.81	0.70	**1.51**

5 Frontier orbitals for isolated molecules

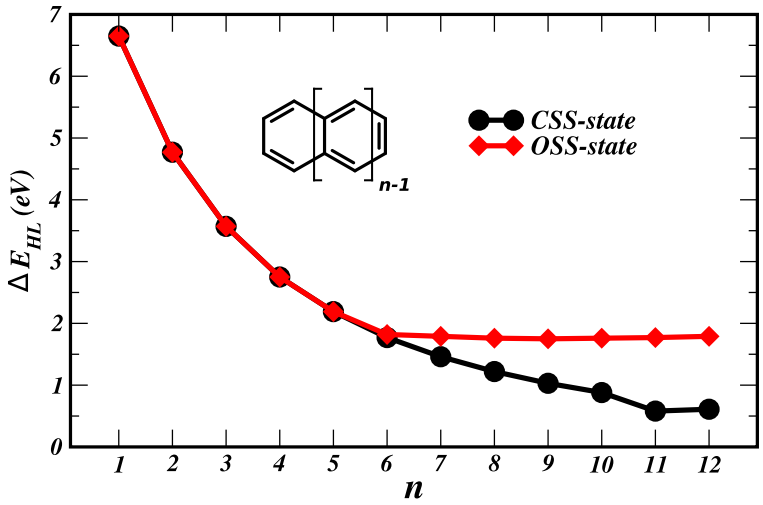

Figure S1: Computed HOMO-LUMO gap (in eV) in CSS state (black curve) and OSS state (red curve) for isolated acenes. In CSS state, HLG shows a steady decay while in OSS state, it saturates ta a constant value of $\sim$ 1.70 eV.

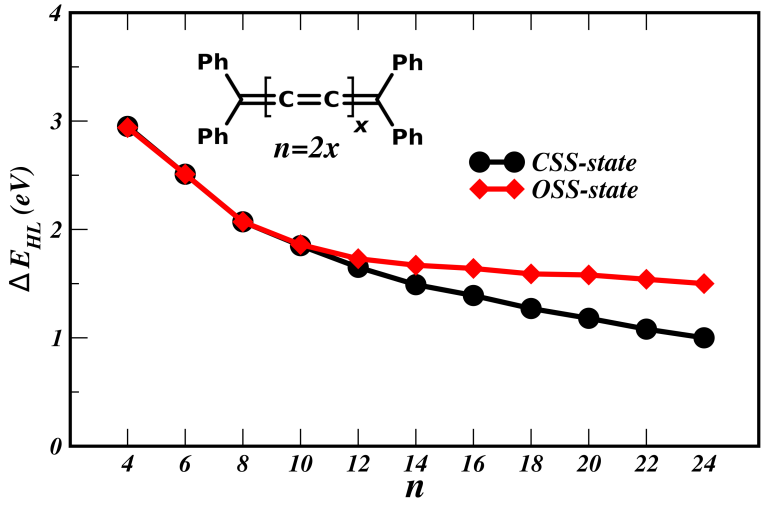

Figure S2: Computed HOMO-LUMO gap (in eV) in CSS state (black curve) and OSS state (red curve) for phenyl-substituted cumulenes.In CSS state, HLG shows a steady decay while in OSS state, it saturates ta a constant value of $\sim$ 1.50 eV.

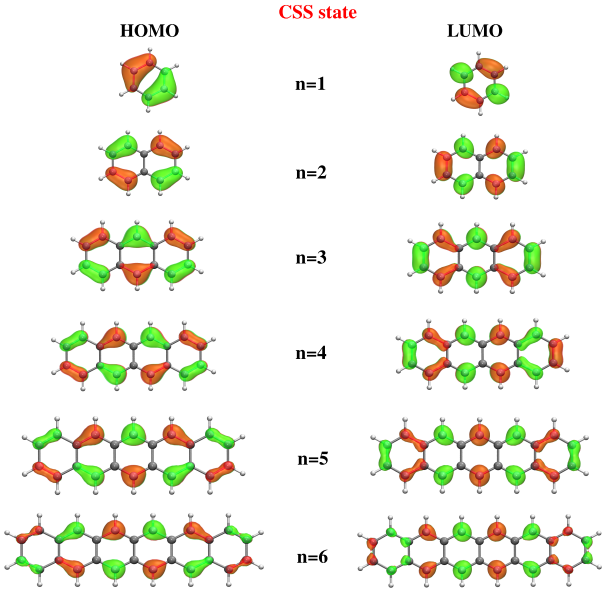

Figure S3: Spatial distribution of frontier HOMO and LUMO for isolated acene series from $n = 1$ to 6 in CSS ground state.

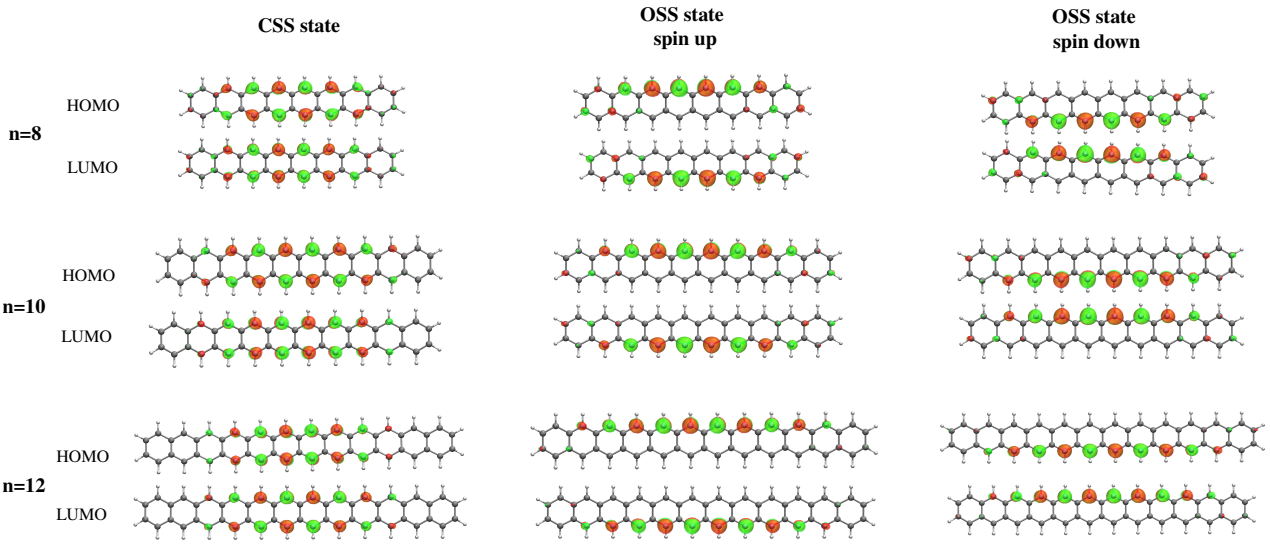

Figure S4: Spatial distribution of frontier HOMO and LUMO for higher acenes in CSS state and both the spin configurations of OSS ground state. In CSS state, MOs are localized at central benzene rings, while in OSS state spin-split orbitals are localized at the opposite ziz-zag edges.

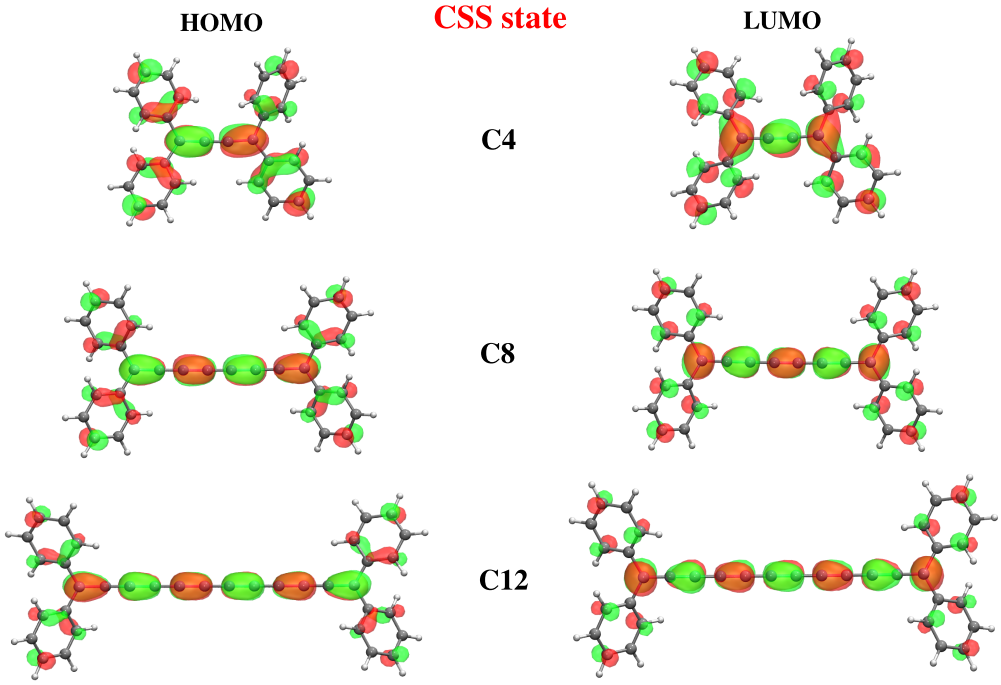

Figure S5: Spatial distribution of frontier HOMO and LUMO for phenyl-substituted cumulene series from C4, C8 and C12 members in CSS ground state.

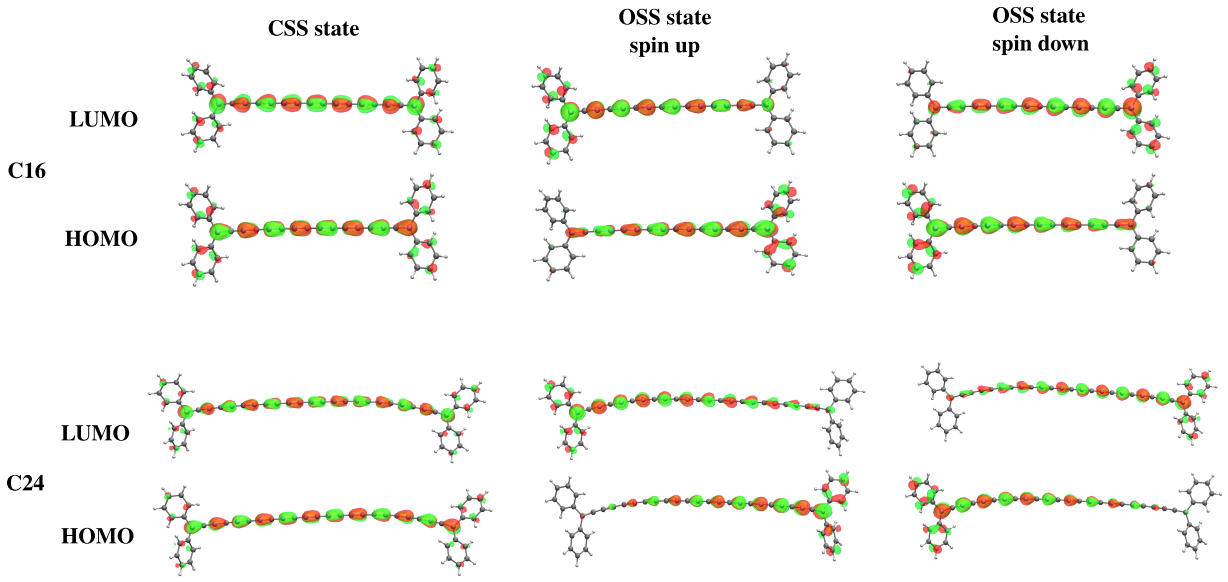

Figure S6: Spatial distribution of frontier HOMO and LUMO for phenyl-substituted cumulenes C16 and C24 members in CSS and both the spin configurations of OSS ground state.

6 Spin density distribution

The spin density distribution for acenes $n = 5$ to 12 in broken symmetry state is shown in Fig. S7. It reveals that acenes features an anti-ferromagnetic coupling of unpaired electrons localized at two opposite edges. For $n = 5$, no spin density appears at the benzene rings, indicating that BS solution do not exists and $n = 5$ is stable in CSS state. Spin density for $n = 6$ illustrates that magnitude of spin moment at the edges is small as compared to n $\geq$ 7, indicating that $n = 6$ case is at borderline in transition from CSS to OSS state.

For phenyl-substituted cumulenes, spin density is uniformly delocalized at the complete molecule (Fig. S8). C10 bears no spin density indicating CSS ground state, while C12 with small spin density is at borderline.

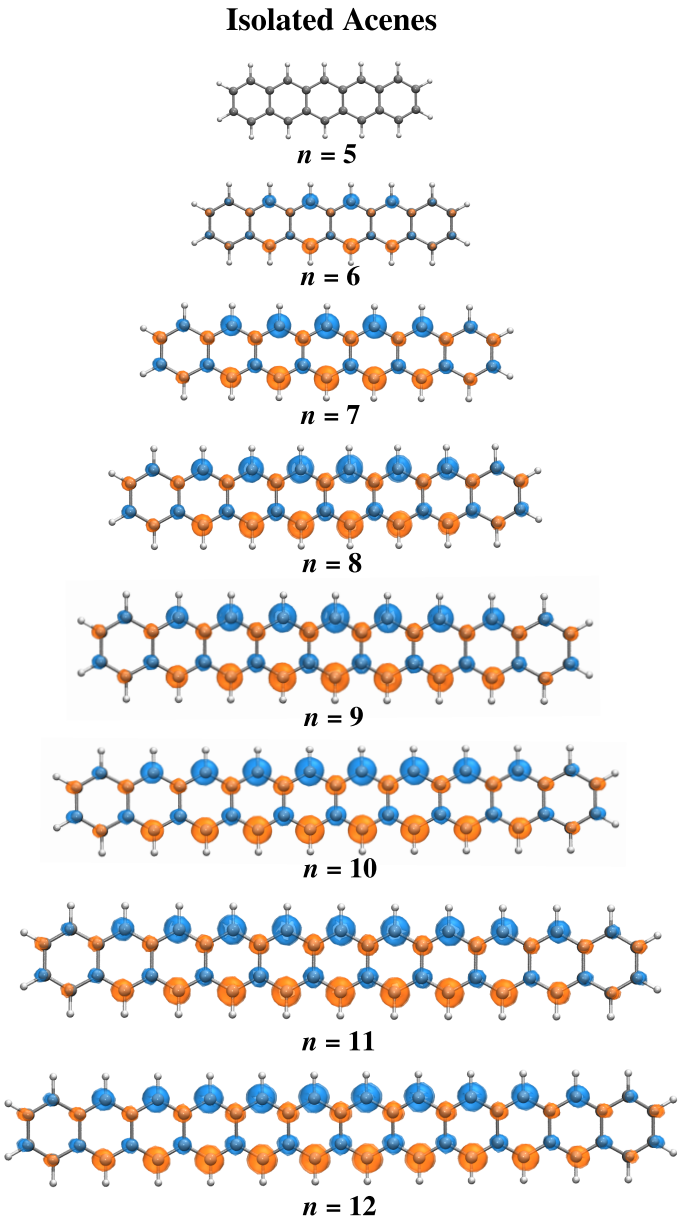

Figure S7: Spin density distribution in BS state for isolated acenes $n = 5$ to 12 computed at UB3LYP/def2-TZVP level. Blue and orange color represents α and β spin with an isovalue of 0.005 $\mu_B/Å^3$. The edges of molecule are spin polarized with equal and opposite magnetic moments at the atoms of upper and lower edges.

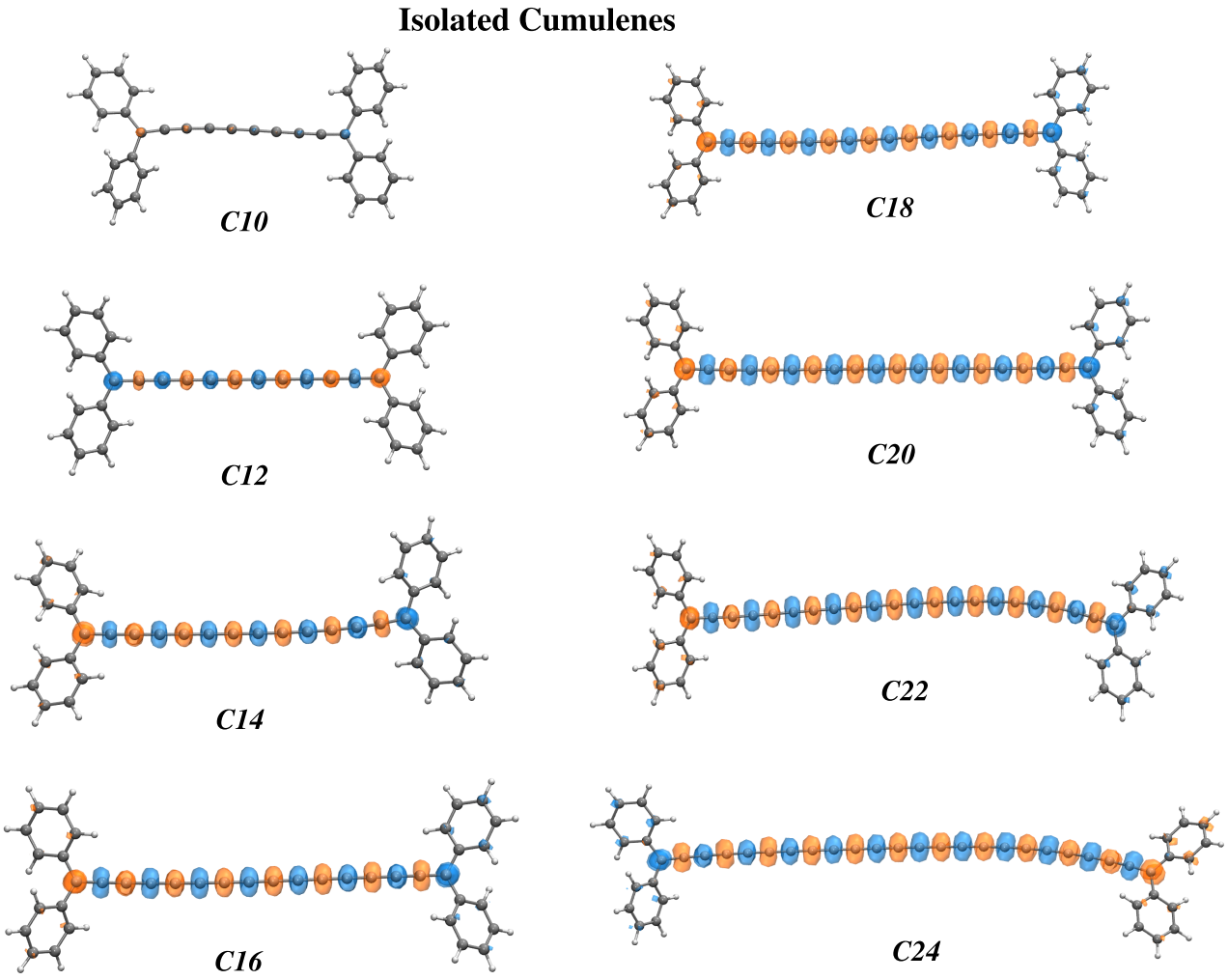

Figure S8: Spin density distribution in BS state for isolated phenyl-substituted cumulenes $n = 10$ to 24 computed at UB3LYP/def2-TZVP level. Blue and orange color represents α and β spin with an isovalue of 0.005 $\mu_B/Å^3$.

7 Energetics of molecular states

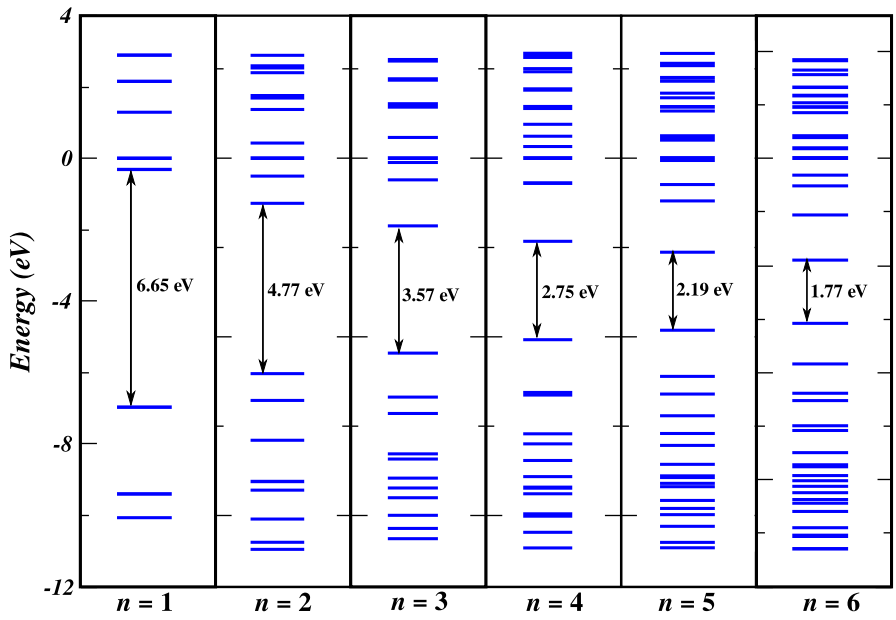

Figure S9: Molecular orbital bands calculated at B3LYP/def2-TZVP level for $n = 1$ to 6 isolated acenes in CSS state within an energy window spanning -11 to 3 eV. Density of molecular levels is increasing with increasing n.

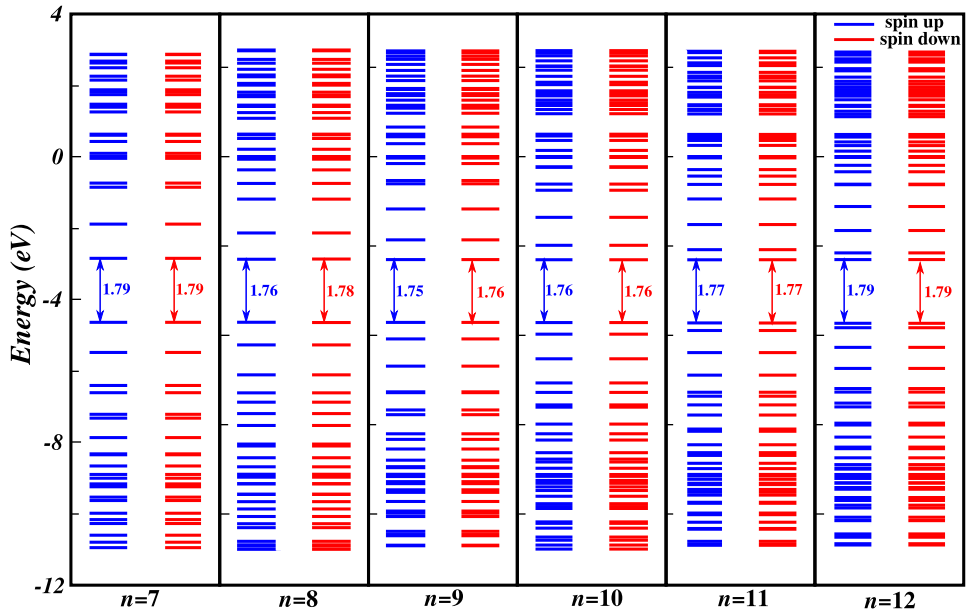

Figure S10: Spin-resolved molecular orbital bands calculated at UB3LYP/def2-TZVP level for $n = 7$ to 12 isolated acenes in OSS ground state within an energy window spanning -11 to 3 eV. Spin-up and spin-down energy levels (shown with blue and red color) are degenerate.

8 CAM-B3LYP computed conductance

Since, LDA based functionals including hybrid functionals tends to suffer from a deficiency of underestimated HOMO-LUMO gap, that contributes to overestimated conductance by these funnctionals. This limitation has been addressed by employing CAM-B3LYP as one of the RSH functional which provides improved agreement to experimental values[14] as compared to B3LYP. As illustrated in Fig. S11, CAM-B3LYP functional provides HOMO-LUMO gap, which is in better agreement to experimental data and our calculated CSSD(T) gaps as compared to B3LYP.

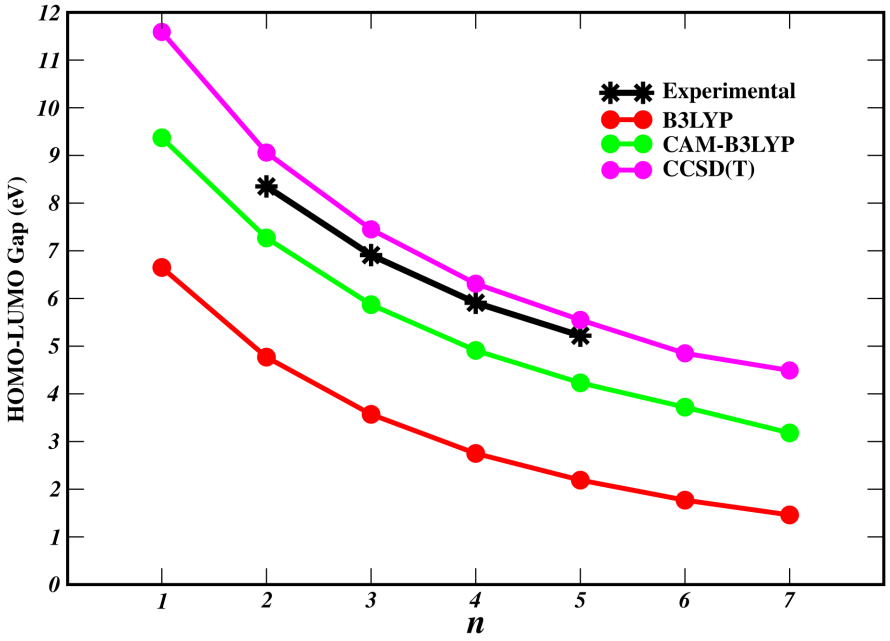

Figure S11: Comparison of computed HOMO-LUMO gaps for n =1 to 7 acenes using hybrid functional B3LYP and range-separated hybrid functional CAM-B3LYP. CCSD(T) gaps are calculated using def2-TZVP basis set. Experimental data is taken from Ref.14.

Table S12: Comparison of computed energies of frontier HOMO and LUMO orbitals and the corresponding energy gap ΔE_{HL} for isolated acenes using B3LYP and CAM-B3LYP in CSS state.

Acenes	**B3LYP**			**CAM-B3LYP**		
n	E(HOMO)	E(LUMO)	ΔE_{HL}	E(HOMO)	E(LUMO)	ΔE_{HL}
1	-6.96	-0.31	**6.65**	-8.49	0.88	**9.37**
2	-6.02	-1.25	**4.77**	-7.42	-0.15	**7.27**
3	-5.45	-1.88	**3.57**	-6.74	-0.87	**5.87**
4	-5.07	-2.32	**2.75**	-6.29	-1.38	**4.91**
5	-4.81	-2.62	**2.19**	-5.97	-1.74	**4.23**
6	-4.61	-2.84	**1.77**	-5.73	-2.01	**3.72**
7	-4.47	-3.01	**1.46**	-5.47	-2.29	**3.18**
8	-4.36	-3.14	**1.22**	-5.30	-2.48	**2.82**
9	-4.27	-3.24	**1.03**	-5.19	-2.61	**2.58**
10	-4.20	-3.32	**0.88**	-5.10	-2.71	**2.39**
11	-4.08	-3.50	**0.58**	-4.74	-3.16	**1.58**
12	-4.10	-3.49	**0.61**	-4.75	3.16	**1.59**

Table S13: Comparison of computed energies of frontier HOMO and LUMO orbitals and the corresponding energy gap ΔE_{HL} for phenyl substituted isolated cumulenes using B3LYP and CAM-B3LYP in CSS state.

Cumulenes	**B3LYP**			**CAM-B3LYP**		
	E(HOMO)	E(LUMO)	ΔE_{HL}	E(HOMO)	E(LUMO)	ΔE_{HL}
C4	-5.26	-2.31	**2.94**	-6.50	-1.40	**5.10**
C6	-5.19	-2.68	**2.51**	-6.37	-1.86	**4.51**
C8	-5.10	-3.02	**2.07**	-6.22	-2.29	**3.92**
C10	-5.07	-3.22	**1.85**	-6.15	-2.52	**3.63**
C12	-5.05	-3.39	**1.65**	-6.10	-2.74	**3.35**
C14	-5.03	-3.54	**1.49**	-6.05	-2.93	**3.11**
C16	-5.03	-3.64	**1.39**	-6.03	-3.06	**2.97**
C18	-5.02	-3.74	**1.27**	-6.00	-3.18	**2.82**
C20	-5.02	-3.83	**1.18**	-5.98	-3.28	**2.70**
C22	-5.01	-3.92	**1.08**	-5.94	-3.39	**2.55**
C24	-5.00	-3.99	**1.00**	-5.93	-3.48	**2.44**

Proceeding towards conductance calculations, we begin by benchmarking against experimental STM-BJ measurements for lower cumulenes. Table S14 illustrates the computed conductance using B3LYP and CAM-B3LYP methods and experimentally reported values by Zang et al.[15] It reveals that CAM-B3LYP based values are within 1 order of magnitude of the experimental values, whereas B3LYP values overestimate the conductance by upto 2 orders of magnitude. Overall, CAM-B3LYP values overestimate the conductance by a factor of ~ 4, as compared to factor of ~ 20 for B3LYP. This improved conductance with CAM-B3LYP is directly understood from the HOMO-LUMO gap (Table S13), which is larger for CAM-B3LYP as compared to B3LYP. Thus, an improved quantitative description of conductance can be obtained with CAM-B3LYP.

Table S14: Comparison of computed conductance (G in units of G_0) for phenyl-substituted cumulenes using B3LYP and CAM-B3LYP methods with experimentally reported values.

Cumulenes	$G(G_0)$		
	B3LYP	**CAM-B3LYP**	**Experiment**[a]
C4	1.31×10^{-2}	3.02×10^{-3}	6.40×10^{-4}
C6	1.26×10^{-2}	2.57×10^{-3}	7.40×10^{-4}
C8	1.72×10^{-2}	2.95×10^{-3}	8.31×10^{-4}

[a] Experimental values are taken from Ref.15.

We next consider the trend of molecular conductance v/s length using B3LYP and CAM-B3LYP in CSS state. As illustrated in Fig. S12, an underestimated orbital gap associated with B3LYP yields an expected overestimated conductance about 2 orders of magnitude higher than CAM-B3LYP. This is reflected in the form of higher β values with CAM-B3LYP.

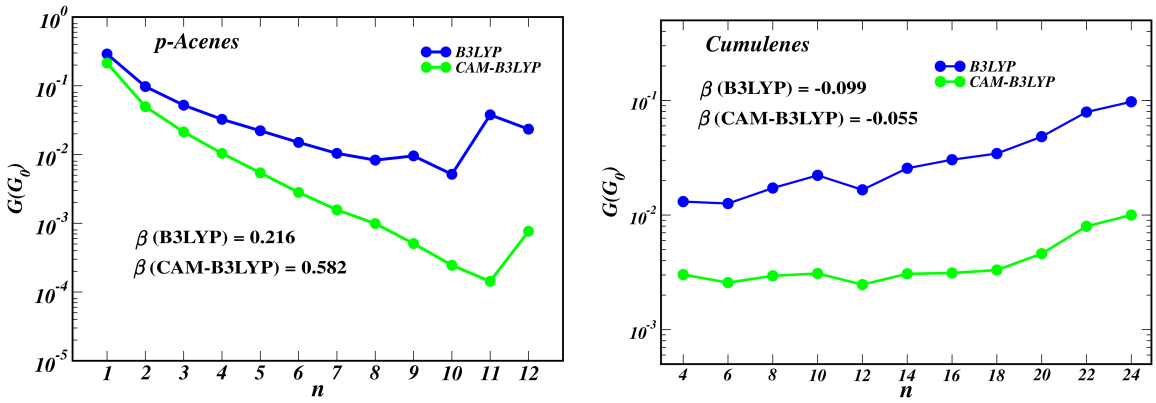

Figure S12: Computed molecular conductance using B3LYP and CAM-B3LYP for p-acenes (left panel) and phenyl-substituted cumulenes (right panel). CAM-B3LYP results in larger β values as compared to B3LYP.

Fig. S13 and Fig. S14 illustrates the evolution of conductance in CSS and OSS state for p-acenes and phenyl-substituted cumulenes using CAM-B3LYP. It reveals that overall qualitative trends for both acenes and cumulenes are preserved with both B3LYP and CAM-B3LYP methods. Cumulenes yields inverted β values in CSS and OSS state, while acenes results in a decaying conductance in both CSS and OSS state, accompanied by a larger resistance in OSS state.

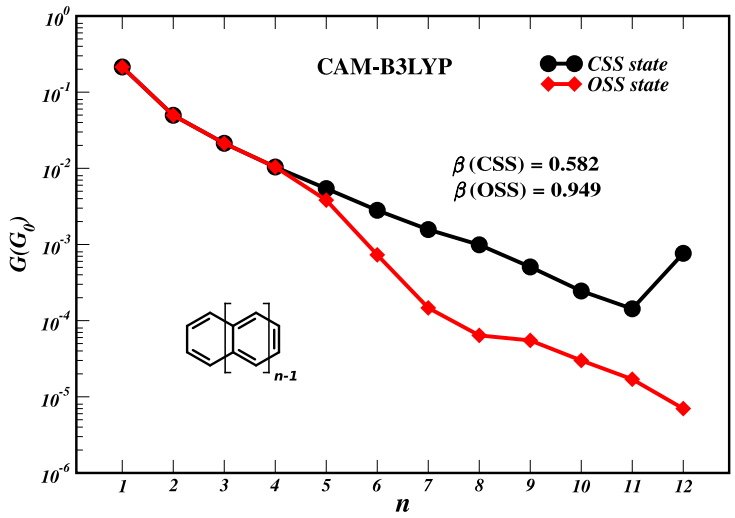

Figure S13: Molecular conductance (in units of G_0) v/s number of phenyl rings n in CSS state (black curve) and OSS state (red curve) for p-acenes using CAM-B3LYP method.

Although CAM-B3LYP succeeds in providing better HOMO-LUMO gaps and consequent better conductance values as compared to B3LYP, however, the performance of CAM-B3LYP for open shell singlets is still inferior as compared to traditional B3LYP. The computed $< S^2 >$ values in BS state (Table S15) shows that CAM-B3LYP yields large $< S^2 >$ values as compared to B3LYP, which even exceeds 2.00 for higher acenes. The similar scenario is observed for higher cumulenes with $< S^2 >$ values reaching to 2.84 for $C24$ cumulene (Table S16). This indicates that CAM-B3LYP suffers from severe spin contamination. The high spin contamination eventually results into the emergence of open shell singlet as a ground state from n=5 onwards, which is in contrast to the reported CSS ground state in literature.

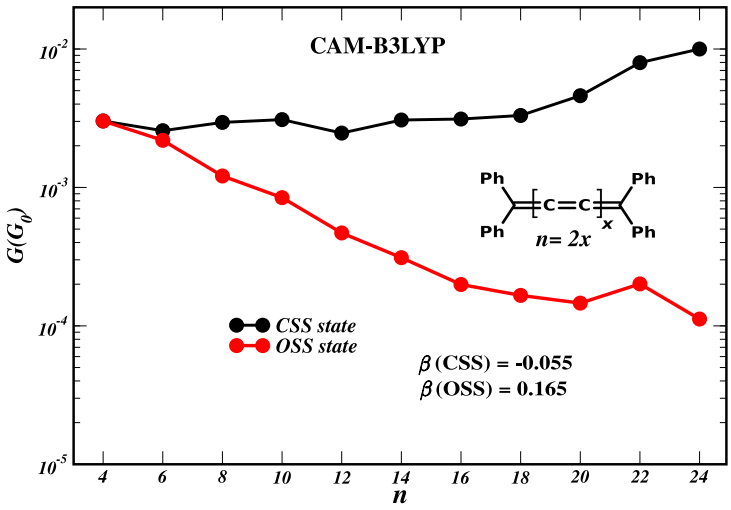

Figure S14: Molecular conductance (in units of G_0) v/s number of C-atoms n in CSS state (black curve) and OSS state (red curve) for phenyl-substituted cumulenes CAM-B3LYP method.

Table S15: Comparison of $< S^2 >$ values in broken-symmetry state for isolated acenes using B3LYP and CAM-B3LYP.

Acenes (n)	$< S^2 >_{BS}$	
	B3LYP	**CAM-B3LYP**
1	0.00	0.00
2	0.00	0.00
3	0.00	0.00
4	0.00	0.00
5	0.00	0.25
6	0.15	0.70
7	0.77	1.17
8	1.07	1.45
9	1.24	1.68
10	1.39	1.92
11	1.54	2.18
12	1.71	2.44

Table S16: Comparison of $< S^2 >$ values in broken-symmetry state for phenyl substituted isolated cumulenes using B3LYP and CAM-B3LYP.

Cumulenes	$< S^2 >_{BS}$	
	B3LYP	**CAM-B3LYP**
C4	0.00	0.00
C6	0.00	0.08
C8	0.00	0.49
C10	0.01	0.77
C12	0.15	1.09
C14	0.37	1.43
C16	0.54	1.73
C18	0.72	2.02
C20	0.91	2.31
C22	1.09	2.58
C24	1.26	2.84

9 Bond Length Alternation

Apart from the electronic structure, we also investigated the structural traits by examining the bond length alternation (BLA) trends for cumulenes and acenes. We compared the B3LYP/def2-TZVP geometries in CSS and OSS state for $n = 20$ cumulene and $n = 10$ acene. For cumulenes, the bond length alternation (shown in Fig. S15 for n=20), reveals that cumulene has the longest bond at the edges and the shortest bond in the middle. This reverse bond length alternation (BLA) prevails in both CSS and OSS state for cumulenes. More interestingly, cumulenes reveals an increased reverse BLA in OSS state as compared to CSS state. In the OSS state, the edge bonds are longer and the central bonds are shorter than in CSS state.

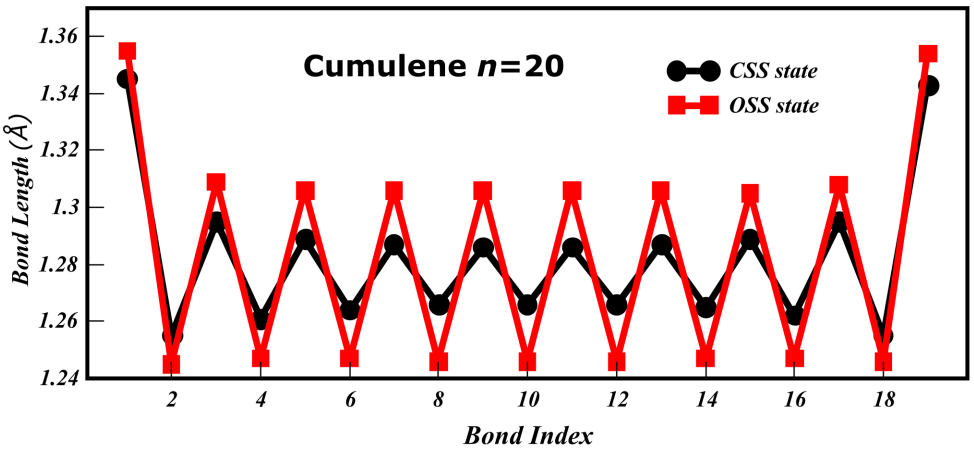

Figure S15: Calculated bond lengths (in Å) for $n = 20$ cumulene using B3LYP/def2-TZVP method in CSS (black curve) and OSS (red curve) optimized geometry.

For polyacenes, the change in transannular bond lengths along the chain of decacene is shown in Fig. S16a, while Fig. S16b displays the C-C bond lengths along the upper zigzag edge (which is mirror-symmetric with the lower edge) for CSS and OSS states. The bond length alternation is insignificant for transannular bonds and C-C bond lengths vary only slightly in the middle rings. The zigzag bonds exhibits shortest bonds at edges in CSS as well as OSS state. This normal BLA in zigzag bonds of polyacenes is in contrast to the reverse BLA observed in cumulenes. As reported previously,[15,16] the reverse BLA in cumulenes is most likely one of the dominant factor driving cumulenes (not acenes) into anti-ohmic regime.

Further, the normal BLA prevailing at the edge bonds of acenes slightly decreases in OSS state. The longer edge bonds shortens slightly while the shorter edge bonds is slightly elongated in OSS state. This eventually results in modest decrease of normal BLA for zigzag bonds in OSS as compared to CSS state. To summarize, the reverse BLA increases in cumulenes on moving from CSS to OSS state. While in acenes, the normal BLA slightly decreases in OSS state.

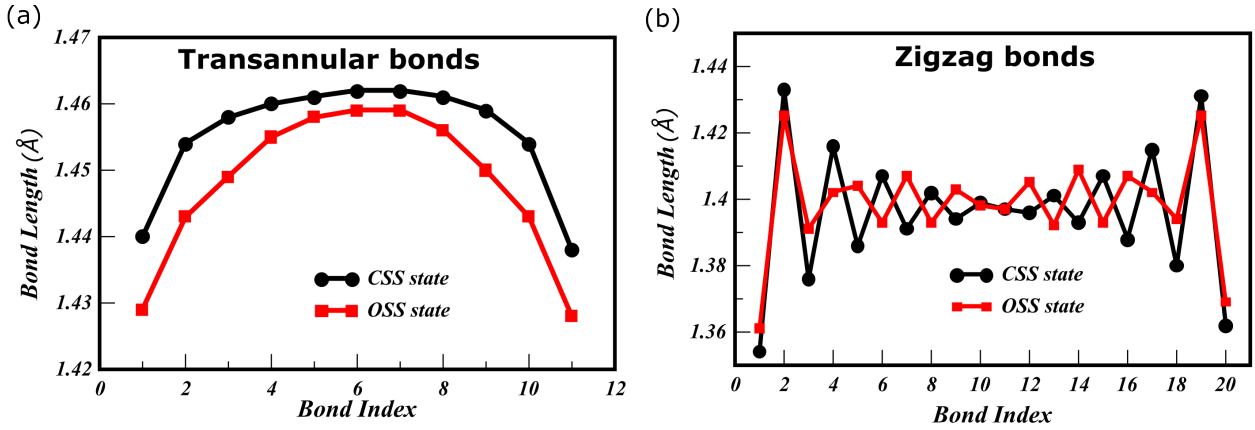

Figure S16: Calculated bond lengths (in Å) for $n = 10$ acene (a) transannular bonds, (b) zigzag bonds using B3LYP/def2-TZVP method in CSS (black curve) and OSS (red curve) optimized geometry.

References

(1) Beck, A. D. Density-functional thermochemistry. III. The role of exact exchange. *J. Chem. Phys* **1993**, *98*, 5648–6.

(2) Weigend, F.; Ahlrichs, R. Balanced basis sets of split valence, triple zeta valence and quadruple zeta valence quality for H to Rn: Design and assessment of accuracy. *Phys. Chem. Chem. Phys.* **2005**, *7*, 3297–3305.

(3) Neese, F. The ORCA program system. *Wiley Interdiscip. Rev. Comput. Mol. Sci.* **2012**, *2*, 73–78.

(4) Neese, F.; Wennmohs, F.; Hansen, A.; Becker, U. Efficient, approximate and parallel Hartree–Fock and hybrid DFT calculations. A chain-of-spheres algorithm for the Hartree–Fock exchange. *Chem. Phys.* **2009**, *356*, 98–109.

(5) Bajaj, A.; Kaur, P.; Sud, A.; Berritta, M.; Ali, M. E. Anomalous Effect of Quantum Interference in Organic Spin Filters. *J. Phys. Chem. C* . **2020**, *124*, 24361–24371.

(6) Bajaj, A.; Khurana, R.; Ali, M. E. Quantum interference and spin filtering effects in photo-responsive single molecule devices. *J. Mater. Chem. C* **2021**, *9*, 11242–11251.

(7) Hay, P. J.; Wadt, W. R. Ab initio effective core potentials for molecular calculations. Potentials for K to Au including the outermost core orbitals. *J. Chem. Phys.* **1985**, *82*, 299–310.

(8) Deffner, M.; Groß, L.; Steenbock, T.; Voigt, B.; Solomon, G.; Herrmann, C. Artaios a code for postprocessing quantum chemical electronic structure calculations. 2010.

(9) Taylor, J.; Guo, H.; Wang, J. Ab initio modeling of quantum transport properties of molecular electronic devices. *Phys. Rev. B* **2001**, *63*, 245407.

(10) Herrmann, C.; Solomon, G. C.; Ratner, M. A. Designing organic spin filters in the coherent tunneling regime. *J. Chem. Phys.* **2011**, *134*, 224306.

(11) Kaur, P.; Ali, M. E. First Principle Investigations of Long-range Magnetic Exchange Interactions via Polyacene Coupler. *Int. J. Quantum Chem.* **2021**, DOI: https://doi.org/10.1002/qua.26756.

(12) Kaur, P.; Ali, M. E. The influence of the radicaloid character of polyaromatic hydrocarbon couplers on magnetic exchange interactions. *Phys. Chem. Chem. Phys.* **2022**, *24*, 13094–13101.

(13) Neaton, J. B.; Hybertsen, M. S.; Louie, S. G. Renormalization of molecular electronic levels at metal-molecule interfaces. *Phys. Rev. Lett.* **2006**, *97*, 216405.

(14) Kadantsev, E. S.; Stott, M.; Rubio, A. Electronic structure and excitations in oligoacenes from ab initio calculations. *J. Chem. Phys.* **2006**, *124*, 134901.

(15) Zang, Y.; Fu, T.; Zou, Q.; Ng, F.; Li, H.; Steigerwald, M. L.; Nuckolls, C.; Venkataraman, L. Cumulene wires display increasing conductance with increasing length. *Nano Lett.* **2020**, *20*, 8415–8419.

(16) Garner, M. H.; Bro-Jørgensen, W.; Pedersen, P. D.; Solomon, G. C. Reverse bond-length alternation in cumulenes: candidates for increasing electronic transmission with length. *J. Phys. Chem. C* . **2018**, *122*, 26777–26789.